

# Gradient-based parameter optimization to determine membrane ionic current composition of human induced pluripotent stem cell-derived cardiomyocytes

**Hirohiko Kohjitani**

Kyoto University Graduate School of Medicine

**Shigeya Koda**

Ritsumeikan University

**Yukiko Himeno**

Ritsumeikan University

**Takeru Makiyama**

Kyoto University Graduate School of Medicine

**Yuta Yamamoto**

Kyoto University Graduate School of Medicine

**Daisuke Yoshinaga**

Kyoto University Graduate School of Medicine

**Yimin Wuriyanghai**

Kyoto University Graduate School of Medicine

**Asami Kashiwa**

Kyoto University Graduate School of Medicine

**Futoshi Toyoda**

Shiga University of Medical Science

**Yixin Zhang**

Ritsumeikan University

**Akira Amano** (✉ [a-amano@fc.ritsumei.ac.jp](mailto:a-amano@fc.ritsumei.ac.jp))

Ritsumeikan University

**Akinori Noma**

Ritsumeikan University

**Takeshi Kimura**

Kyoto University Graduate School of Medicine

**Keywords:** Parameter optimization method, hiPSC-CMs, Cardiac action potential, Mathematical model, Computer simulation

**Posted Date:** July 5th, 2022

**DOI:** <https://doi.org/10.21203/rs.3.rs-1747535/v1>

**License:**  This work is licensed under a Creative Commons Attribution 4.0 International License.

[Read Full License](#)

---

1

2

3

4 **Gradient-based parameter optimization to determine membrane ionic current composition of human**  
5 **induced pluripotent stem cell-derived cardiomyocytes**

6

7 Hirohiko Kohjitani<sup>1</sup>, Shigeeya Koda<sup>2</sup>, Yukiko Himeno<sup>2</sup>, Takeru Makiyama<sup>1</sup>, Yuta Yamamoto<sup>1</sup>, Daisuke

8 Yoshinaga<sup>3</sup>, Yimin Wuriyanghai<sup>1</sup>, Asami Kashiwa<sup>1</sup>, Futoshi Toyoda<sup>4</sup>, Yixin Zhang<sup>2</sup>, Akira Amano<sup>2</sup>, Akinori

9 Noma<sup>2</sup>, Takeshi Kimura<sup>1</sup>

10

11 <sup>1</sup>Department of Cardiovascular Medicine, Kyoto University Graduate School of Medicine, Kyoto, Japan

12 <sup>2</sup>Graduate School of Life Sciences, Ritsumeikan University, Kusatsu, Japan

13 <sup>3</sup>Department Pediatrics, Kyoto University Graduate School of Medicine, Kyoto, Japan

14 <sup>4</sup>Department of Physiology, Shiga University of Medical Science, Otsu, Japan

15

16 **\* Correspondence:**

17 Akira Amano

18

19 **Keywords: Parameter optimization method, hiPSC-CMs, Cardiac action potential, Mathematical**  
20 **model, Computer simulation**

21

22 **Abbreviations**

23 hiPSC-CMs; human induced pluripotent stem cell-derived cardiomyocytes

24 AP; action potential

25 MDP; the maximum diastolic potential

26 SDD; slow diastolic depolarization

- 27  $I_m$ ; membrane current
- 28  $V_m$ ; membrane voltage
- 29 orp; optimization of randomized model parameters
- 30 PS; pattern search method
- 31 BP; base point for searching minimum MSE in the Pattern Search
- 32 NP; searching point in reference to BP in the Pattern Search
- 33 MSE; mean square error between two different  $V_m$  records
- 34 stp; step size to move NP
- 35 x; subscript to represent membrane current such as  $I_{Na}$ ,  $I_{CaL}$ ,  $I_{K1}$ ,  $I_{ha}$ ,  $I_{Kr}$ ,  $I_{Kur}$ ,  $I_{Ks}$  and  $I_{bNSC}$
- 36

**37 1. Abstract**

38           Premature cardiac myocytes derived from human-induced pluripotent stem cells (hiPSC-CMs) show  
39 heterogeneous action potentials (APs), most probably because of different expression patterns of membrane  
40 ionic currents. We aim to develop a method of determining expression patterns of functional channels in terms  
41 of the whole-cell ionic conductances ( $G_x$ ) using individual spontaneous AP configurations. However, it has  
42 been suggested that apparently identical AP configurations were obtained by different sets of ionic currents in  
43 a mathematical model of cardiac membrane excitation. If so, the inverse problem of  $G_x$  estimation might not be  
44 solved. We computationally tested the feasibility of the gradient-based optimization method. For realistic  
45 examination, conventional 'cell-specific models' were prepared by superimposing the model output of AP on  
46 each experimental AP record by the conventional manual adjustment of  $G_x$ s of the baseline model. Then,  $G_x$ s  
47 of 4 ~ 6 major ionic currents of the 'cell-specific models' were randomized within a range of  $\pm 5 \sim 15\%$  and  
48 were used as initial parameter sets for the gradient-based automatic  $G_x$ s recovery by decreasing the mean  
49 square error (MSE) between the target and model output. When plotted all data points of MSE -  $G_x$  relation  
50 during the optimization, we found that the randomized population of  $G_x$ s progressively converged to the  
51 original value of the cell-specific model with decreasing MSE. To confirm the absence of any other local  
52 minimum in the global search space, we mapped the MSE by randomizing  $G_x$ s over a range of 0.1 ~ 10 times  
53 the control. No additional local minimum of MSE was obvious in the whole parameter space besides the global  
54 minimum of MSE at the default model parameter.

55

**56 2. Introduction**

57           During more than a half-century, the biophysical characteristics of ion transporting molecules  
58 (channels and ion exchangers) have been extensively analyzed, and biophysical models of each functional  
59 component have largely been detailed [1–4] (for human-induced pluripotent stem cells (hiPSC-CMs) see [5–  
60 7]). In addition, various composite cell models, including the membrane excitation, cell contraction, and the  
61 homeostasis of the intracellular ionic composition, have been developed by integrating mathematical models at  
62 molecular levels into the cardiac cell models [8–11]. These models have already been quite useful in

63 visualizing individual currents underlying the action potential (AP) configuration under various experimental  
64 conditions in matured cardiac myocytes. However, the utility of these mathematical cell models has been  
65 limited because of the lack of extensive validation for the accuracy of the model output. This is the drawback  
66 of the subjective manual fitting used in almost all mathematical cardiac cell models so far published. A new  
67 challenge of such mechanistic models of cardiac membrane excitation might be an examination in a very  
68 different paradigm to assess if the large but continuous variety of cardiac AP configurations, for example,  
69 those recorded in the hiPSC-CMs, can be reconstructed by applying the automatic parameter optimization  
70 method to the human cardiac cell models.

71         The automatic parameter optimization technique has been used to determine parameters objectively in  
72 a wide range of various biological models (in cardiac electrophysiology; [12–15], in the systems  
73 pharmacology; [16–20]). Because of this utility, a large variety of improvements have been made in the area of  
74 information technology [21,22]. However, in electrophysiology, it has been suggested that different  
75 combinations of model parameters can produce APs, which are very similar [23–25] (see also [13]). It has been  
76 considered that the determination of current density at high fidelity and accuracy requires additional  
77 improvements to the optimization method in the cardiac cell model because of complex interactions among  
78 ionic currents underlying the membrane excitation (see [26], for review; [23]).

79         The final goal of our study is to develop an objective and accurate method of determining the current  
80 profile (that is, the expression level of functional ionic currents) underlying individual AP configurations. As a  
81 case study, we select a large variety of AP configurations in the hiPSC-CMs, which are difficult to classify into  
82 the conventional nodal-, atrial- or ventricular-types. Nevertheless, it has been clarified that the molecular  
83 bases of the ion channels expressed in the hiPSC-CMs well correspond to those in the adult cardiac  
84 myocytes (GSE154580 [GEO Accession viewer \(nih.gov\)](#)). Thus, we use the human ventricular cell model  
85 (hVC model, [11]) for the baseline model. In the present study, we computationally examine the feasibility of  
86 the basic gradient-based optimization method, pattern search (PS) algorithm [21,27,28] in the model of cardiac  
87 AP generation. We prepared a given AP configuration using each 'cell specific model', which was prepared by  
88 the conventional manual fitting of the hVC model to the respective experimental recordings. To assess the

89 accuracy of the PS method of parameter optimization, this AP waveform generated by the cell-specific model  
90 was used as a target of the optimization. Then, the initial set of parameters for the optimization was prepared  
91 by uniform randomization centered around the model's default values. The PS algorithm should return the  
92 original parameters by decreasing the error function (MSE) between the modified model output and target AP  
93 waveforms. The accuracy of optimization was definitely judged by recovering of the original values of each  
94 ionic current amplitude as the MSE progressively decreased toward zero.

95

### 96 **3. Materials and Methods**

#### 97 **3.1. The baseline model of hiPSC-CM membrane excitation**

98 The baseline model of hiPSC-CMs was essentially the same as the human ventricular cell model (hVC  
99 model), which has been fully described in references [10,11] and shares many comparable characteristics with  
100 other human models so far published [8,9]. The model structure of the hVC model consists of the cell  
101 membrane with a number of ionic channel species and a few ion transporters, the sarcoplasmic reticulum  
102 equipped with the Ca<sup>2+</sup> pump (SERCA), and the refined Ca<sup>2+</sup> releasing units coupled with the L-type Ca<sup>2+</sup>  
103 channels on the cell membrane at the nano-scale dyadic space, the contractile fibers, and the cytosolic three  
104 Ca<sup>2+</sup> diffusion spaces containing several Ca<sup>2+</sup>-binding proteins (Fig S1). All model equations and abbreviations  
105 are in Supplemental Materials.

106 The source code of the present hiPSC-CM model was written in VB.Net and is available from the  
107 archive site (<https://doi.org/10.1101/2022.05.16.492203>).

108

109 The kinetics of the ionic currents in the baseline model were readjusted according to new  
110 experimental measurements if available in the hiPSC-CMs [29] (Fig S2). In the present study, the net  
111 membrane current ( $I_{tot\_cell}$ ) is calculated as the sum of nine ion channel currents and two ion transporters ( $I_{NaK}$   
112 and  $I_{NCX}$ ) (Eq 1).

$$113 \quad I_{tot\_cell} = I_{Na} + I_{CaL} + I_{ha} + I_{K1} + I_{Kr} + I_{Ks} + I_{Kur} + I_{Kto} + I_{bNSC} + I_{NaK} + I_{NCX} \quad Eq \ 1$$

114

115 The membrane excitation of the model is generated by charging and discharging the membrane  
 116 capacitance ( $C_m$ ) by the net ionic current ( $I_{tot\_cell}$ ) across the cell membrane (Eq 2). The driving force for the  
 117 ionic current is given by the potential difference between  $V_m$  and the equilibrium potential ( $E_x$ ) (Eq 3). The net  
 118 electrical conductance of the channel is changed by the dynamic changes in the open probability ( $pO$ ) of the  
 119 channel, which is mostly  $V_m$ -dependent through the  $V_m$ -dependent rate constants ( $\alpha, \beta$ ) of the opening and  
 120 closing conformation changes of the channel (Eqs 4 and 5).

$$121 \quad \frac{dV_m}{dt} = -\frac{I_{tot\_cell}}{C_m} = -\frac{\sum I_x}{C_m} \quad \text{Eq 2}$$

$$122 \quad I_x = \bar{G}_x \cdot pO \cdot (V_m - E_x) \quad \text{Eq 3}$$

$$123 \quad \frac{dpO}{dt} = \alpha \cdot (1 - pO) - \beta \cdot pO \quad \text{Eq 4}$$

$$124 \quad [\alpha \ \beta]^T = f(V_m) \quad \text{Eq 5}$$

125 The exchange of  $3Na^+ / 2K^+$  by the Na/K pump and the  $3Na^+ / 1Ca^{2+}$  exchange by the NCX also  
 126 generate sizeable fractions of membrane ionic current,  $I_{NaK}$ , and  $I_{NCX}$ , respectively. We excluded background  
 127 currents of much smaller amplitude, such as  $I_{KACH}$ ,  $I_{KATP}$ ,  $I_{LCCa}$  and  $I_{Cab}$ , from the parameter optimization and  
 128 adjusted only the non-selective background cation current ( $I_{bNSC}$ ) of significant amplitude for the sake of  
 129 simplicity [30–32]. The  $I_{bNSC}$  is re-defined in the present study as a time-independent net current, which  
 130 remained after blocking all time-dependent currents.

131

### 132 **3.2. The computational parameter optimization**

133 The whole cell conductance  $G_x$  of a given current system ( $x$ ) is modified by multiplying the limiting  
 134 conductance  $\bar{G}_x$  (Eq 3) of the baseline model by a scaling factor  $sf_x$  (Eq 6) and are used for the parameter  
 135 optimization.

$$136 \quad G_x = \bar{G}_x \cdot sf_x \quad \text{Eq 6}$$

137 The mean square error (MSE) function (Eq 7) was used in the parameter optimization, where  $V_{m,a}$   
 138 represents adaptive  $V_m$  (the model output) generated by adjusting  $sf_x$ s of the baseline model. The target  $V_{m,t}$   
 139 represents the AP of the intact baseline model.

140

$$MSE = \frac{\sum(V_{m,a} - V_{m,t})^2}{N}$$

Eq 7

141 The MSE was stabilized by obtaining a quasi-stable rhythm of spontaneous APs through continuous  
142 numerical integration of the model, usually 30 ~ 100 spontaneous cycles were calculated for a new set of  $sf_x$ s.  
143 The MSE was calculated within a time window. The width of this time window was adjusted according to the  
144 AP phase of interest. N is the number of digitized  $V_m$  points with a time interval of 0.1 ms.

145 In the usual parameter optimization, the  $V_{m,a}$  is generated by modifying the baseline model for  
146 comparison with the experimental record ( $V_{m,t} = V_{m,rec}$ ). However, to evaluate the identifiability of the  
147 parameter optimization, a simple approach was taken in the present study. Namely, we used the manually  
148 adjusted 'cell-specific' model for the target ( $V_{m,t}$ ), which was nearly identical to  $V_{m,rec}$ . More importantly, the  
149 'cell-specific'  $V_m$  is totally free from extra-fluctuations (noise), which were observed in almost all AP  
150 recordings in hiPSC-CMs. In the optimization process, the initial value of each optimization parameter was  
151 prepared by randomizing the  $sf_x$ s of the cell-specific model by  $\pm 5\sim 15\%$  at the beginning of each run of PS  
152 ( $V_{m,orp}$ ) in Eq 8 and the PS runs of several hundred were repeated. Thus, the error function is,

153

$$MSE = \frac{\sum(V_{m,orp} - V_{m,t})^2}{N}$$

Eq 8

154 We call this optimization method 'orp test' in the present study.

155 The advantage of using a manually adjusted cell model for the optimization target is that the accuracy  
156 of parameter optimization is proved by recovering all  $sf_x = 1$  independently from the randomized initial  
157 parameter set. Note the same approach was used in [23] in evaluating the accuracy of the parameter  
158 optimization by applying the genetic algorithm (GA) to the TNNP model of the human ventricular cell [33].

159 The optimization of using the randomized initial model parameters were repeated for more than 200  
160 runs. Thus, the orp test might be classified in a 'multi-run optimization'. The distribution of the  $sf_x$  data points  
161 obtained during all test runs was plotted in a single  $sf_x$ -MSE coordinate to examine the convergence of  
162 individual  $sf_x$ s with the progress of the orp test.

163

164 **3.3. The pattern search method for the optimization**

165 For a system showing the relatively simple gradient of MSE along the parameter axis, the gradient-  
166 based optimization methods are more efficient in general than the stochastic methods for this kind of objective  
167 function. We used one of the basic gradient-based optimization methods, the PS algorithm. The computer  
168 program code of the pattern search [34] is simple (see Supplemental Materials) and does not require  
169 derivatives of the objective function. We implemented the code into a homemade program for data analysis (in  
170 VB) to improve the method for better resolution and to save computation time.

171 The primary PS method uses a base and new points [27]. In brief,  $sf_x$  is coded with symbols  $BP_x$  and  
172  $NP_x$  in the computer program, representing a base point ( $BP_x$ ) and a new searching point ( $NP_x$ ), respectively.  
173 Namely, MSE is calculated on each movement of  $NP_x$  by adding or subtracting a given step size ( $stp$ ) to the  
174  $BP_x$ , and the search direction is decided by the smaller MSE. Then, the whole mathematical model is  
175 numerically integrated (Eqs 2, 3, 4, and 5) using  $NP_x$  to reconstruct the time course of AP ( $V_{m,a}$ ). This  
176 adjustment is conducted sequentially for each of the 4~6 selected currents in a single cycle of optimization.  
177 The cycle is repeated until no improvement in MSE is gained by a new set of  $NP_x$ s. Then, the  $BP_x$  set is  
178 renewed by the new set of  $NP_x$  for the subsequent series of optimization. Simultaneously, the  $stp$  is reduced by  
179 a given reduction factor ( $redFct$  of 1/4). The individual PS run is continued until the new  $stp$  becomes smaller  
180 than the critical  $stp$  ( $crtstp$ ), which is set to  $2\sim 10 \times 10^{-5}$  in the present study.

181

182 **3.4. Selection of ionic currents for the optimization**

183 When we get a new experimental record of AP, we do not start the analysis with an automatic  
184 optimization of  $G_x$  but first adjust the baseline model by conducting the conventional manual fitting. The nine  
185 ionic currents in Eq 1 in the baseline model are adjusted bit by bit to superimpose the simulated AP on the  
186 experimental one. During this step, it is important to pay attention to the influences of each  $sf_x$  adjustment on  
187 the simulated AP configuration on the computer display. Thereby, one may find several key current  
188 components which should be used in the automatic parameter optimization. Usually, currents showing a

189 relatively large magnitude of  $G_x$  were selected for the automatic optimization according to Eq 2, while those  
 190 which scarcely modified the simulated AP were left as default values in the baseline model.

191

### 192 **3.5. Principal component analysis of the cell-specific models**

193 When the orp test is conducted with  $p$  elements, it is possible to record the final point BP where the  
 194 MSE is improved in the  $p$ -dimensional space. Suppose we represent the matrix when  $n$  data points are acquired  
 195 as an  $n \times p$  matrix  $X$ . In that case, we obtain a vector space based on the unit vector that maximizes the  
 196 variance (first principal component: PC1) and the  $p$ -dimensional unit vector orthogonal to it (loadings vector  
 197  $\mathbf{w}_{(k)} = (w_1, w_2 \dots, w_p)$ ). It is possible to convert each row,  $\mathbf{x}_{(i)}$  of the data matrix  $X$  into a vector of principal  
 198 component scores,  $\mathbf{t}_{(i)}$ . The transformation is defined by

$$199 \quad \mathbf{t}_{k(i)} = \mathbf{x}_{(i)} \cdot \mathbf{w}_{(k)} \quad \text{for } i = 1, 2, \dots, n \quad k = 1, 2, \dots, p \quad \text{Eq 9}$$

200 In order to maximize variance, the first weight vector  $\mathbf{w}_{(1)}$  corresponding to the first principal  
 201 component thus has to satisfy,

$$202 \quad \mathbf{w}_{(1)} = \arg \max_{\mathbf{w}} \left\{ \frac{\mathbf{w}^T \mathbf{X}^T \mathbf{X} \mathbf{w}}{\mathbf{w}^T \mathbf{w}} \right\} \quad \text{Eq 10}$$

203 The  $k$ -th component can be found by subtracting the first  $(k-1)$ -th principal components from  $X$

$$204 \quad \widehat{\mathbf{X}}_k = \mathbf{X} - \sum_{s=1}^{k-1} \mathbf{X} \mathbf{w}_{(s)} \mathbf{w}_{(s)}^T \quad \text{Eq 11}$$

205 Then the weight vector is given as a vector such that the variance of the principal component scores is  
 206 maximized for the new data matrix.

$$207 \quad \mathbf{w}_{(k)} = \arg \max_{\mathbf{w}} \left\{ \frac{\mathbf{w}^T \widehat{\mathbf{X}}_k^T \widehat{\mathbf{X}}_k \mathbf{w}}{\mathbf{w}^T \mathbf{w}} \right\} \quad \text{Eq 12}$$

208

### 209 **3.6. Membrane excitation and its cooperativity with intracellular ionic dynamics**

210 When any of  $G_{x,s}$  is modified, the intracellular ion concentrations ( $[\text{ion}]_i$ ) change, although the  
 211 variation is largely compensated for with time in intact cells through modification of the activities of both  
 212  $3\text{Na}^+/2\text{K}^+$  pump (NaK) and  $3\text{Na}^+/1\text{Ca}^{2+}$  exchange (NCX). In the present study, we imitated this long-term

213 physiological homeostasis of  $[ion]_i$  by introducing empirical Eqs 13 and 14. These equations induced 'negative  
 214 feedback' to the capacity ( $maxI_{NaK}$  and  $maxI_{NCX}$ ) of these ion transporters. Namely, each correcting factor ( $crf_x$ )  
 215 was continuously scaled to modify the limiting activity of the transporters to keep the  $[Na^+]_i$  or the total  
 216 amount of Ca within the cell ( $Ca_{tot}$ ) equal to their pre-set level ( $stdNa_i$ ,  $stdCa_{tot}$ ) with an appropriate delay  
 217 (coefficients 0.3 and 0.008 in Eqs 13 and 14, respectively).

218 For the control of  $[Na^+]_i$ ,

$$219 \quad \begin{aligned} \Delta crf_{NaK} &= -(stdNa_i - Na_i) \times 0.3, & stdNa_i &= 6.1mM, \\ I_{NaK} &= (crf_{NaK} \cdot maxI_{NaK}) \cdot vcy_{NaK} \end{aligned} \quad \text{Eq 13}$$

220 For the control of  $Ca_{tot}$ ,

$$221 \quad \begin{aligned} \Delta crf_{NCX} &= -(stdCa_{tot} - Ca_{tot}) \times 0.008, & stdCa_{tot} &= 79amol, \\ I_{NCX} &= (crf_{NCX} \cdot maxI_{NCX}) \cdot (k_1 \cdot E_{1Na} \cdot E_{1NCX} - k_2 \cdot E_{2Na} \cdot E_{2NaCa}) \end{aligned} \quad \text{Eq 14}$$

222 The  $Ca_{tot}$  is given by  $[Ca]_i$  included in the cytosolic three Ca-spaces *jnc*, *iz*, and *blk*, and in the  
 223 sarcoplasmic reticulum  $SR_{up}$  and  $SR_{rl}$  in the free or bound forms, respectively.

$$224 \quad Ca_{tot} = [Ca_{tot}]_{jnc} \cdot vol_{jnc} + [Ca_{tot}]_{iz} \cdot vol_{iz} + [Ca_{tot}]_{blk} \cdot vol_{blk} + [Ca_{tot}]_{SR_{up}} \cdot vol_{SR_{up}} + [Ca_{tot}]_{SR_{rl}} \cdot vol_{SR_{rl}} \quad \text{Eq 15}$$

225 Here, the *vol* is the volume of the cellular Ca compartment (see more detail, [11]).

226

### 227 **3.7. Preparation of dissociated hiPSC-CMs and recording of spontaneous APs**

228 201B7 and 253G1 hiPSC lines generated from a healthy individual were used in this study (Takahashi  
 229 et al. 2006, Nakagawa et al. 2008). Differentiation of hiPSCs into cardiomyocytes was promoted using an  
 230 embryoid body (EB) differentiating system (Yang et al. 2008). hiPSC were incubated at 37 °C in 5% CO<sub>2</sub>, 5%  
 231 O<sub>2</sub>, and 90% N<sub>2</sub> for the first 12 days to promote differentiation. The hiPSCs aggregated to form EBs and were  
 232 cultured in suspension for 20 days. On the 20th day of culture, EBs were treated with collagenase B (Roche,  
 233 Basel, Switzerland) and trypsin EDTA (Nacalai Tesque, Kyoto, Japan) and dispersed into single cells or small  
 234 clusters, which were plated onto 0.1% gelatin-coated dishes. hiPSC-CMs were then maintained in a  
 235 conditioned medium. The experimental study using the hiPSC-CMs was approved by the Kyoto University  
 236 ethics review board (G259) and conformed to the principles of the Declaration of Helsinki.

237

238 **3.8. Electrophysiological recordings of hiPSC-CM APs**

239 For single-cell patch-clamp recordings, gelatin-coated glass coverslips were placed into each well of a  
240 6-well plate, and 2 ml of DMEM/F12 containing 2% FBS and 80,000-120,000 CMs were added in each well.  
241 Spontaneous APs were recorded from beating single CM using the perforated patch-clamp technique with  
242 amphotericin B (Sigma-Aldrich) at  $36 \pm \text{one } ^\circ\text{C}$ . Data were acquired at 20 kHz with the Multiclamp 700B  
243 amplifier (Molecular Devices, Sunnyvale, CA, USA), Digidata 1440 digitizer hardware (Molecular Devices),  
244 and pClamp 10.4 software (Molecular Devices). The glass pipettes had a resistance of 3-6 M $\Omega$  after filling  
245 them with the intracellular solution. The external solution used for AP recordings was composed of the  
246 following composition (in mM): NaCl 150, KCl 5.4, CaCl<sub>2</sub> 1.8, MgCl<sub>2</sub>-6H<sub>2</sub>O 1, glucose 15, HEPES 15, and  
247 Na-pyruvate 1; pH was adjusted to 7.4 by titrating NaOH. Intracellular solution contained (in mM): KCl 150,  
248 NaCl 5, CaCl<sub>2</sub> 2, EGTA 5, MgATP 5, HEPES 10 (pH adjusted to 7.2 with KOH), and amphotericin B 300  
249  $\mu\text{g/ml}$ .

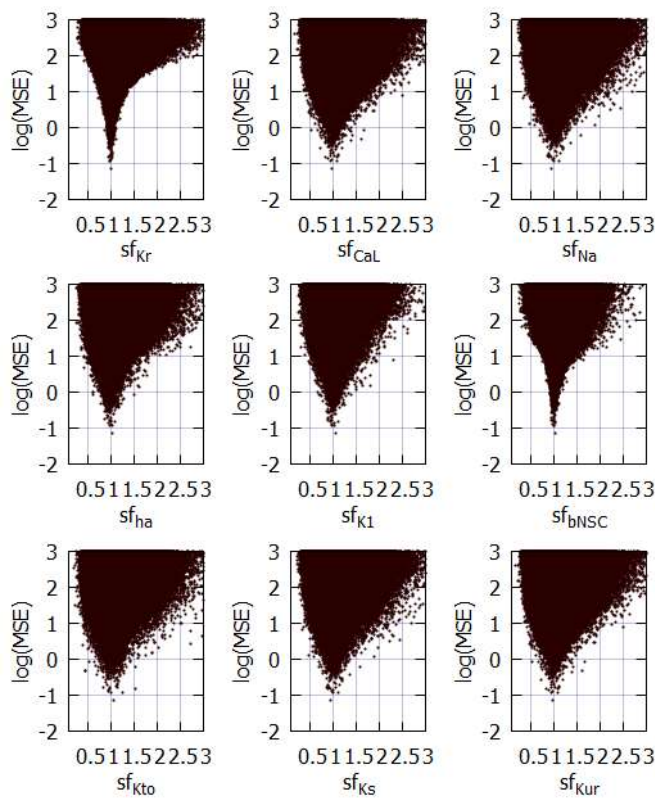
250

251 **4. Results**

252 **4.1. Mapping the magnitude of MSE over the nine global parameter space**

253 Parameter identifiability has been one of the central issues in the parameter optimization of biological  
254 models [14,20]. For confirmation of the identifiability of a unique set of solutions using the parameter  
255 optimization method, mapping of the MSE distribution is required over an enlarged parameter space defined  
256 by the  $sf_x$  of the nine ionic currents of the baseline model. The randomization of  $sf_x$  ranged from 1/10 to  $\sim 10$   
257 times the default values, and the calculation was performed for  $\sim 5,000,000$  sets, as shown in Fig 1, where  
258 magnitudes of  $\log(MSE)$  were plotted against each  $sf_x$  on the abscissa.

259 The data points of MSE at a given  $sf_x$  include all variable combinations of the other eight  $sf_s$ s. The  
 260 algorithm of the PS method searches for a parameter set, which gives the minimum MSE at a given  $stp$  through  
 261 the process of optimization. Although drawing a clear envelope curve by connecting the minimum MSEs at  
 262 each  $sf_x$  was difficult because of the insufficient number of data points in these graphs (Fig 1), an approximate  
 263 envelope of the minimum MSEs may indicate a single global minimum of MSE located at the control  $sf_x$



equals one, as typically exemplified by  $I_{Kr}$ - and  $I_{bNSC}$ -MSE relations. On both sides of the minimum, steep slopes of  $MSE/sf_x$  are evident in all graphs. Outside this limited  $sf_x$ -MSE area, the global envelope showed a gentle and monotonic upward slope toward the limit on the right side. No local minimum was observed in all of the  $sf_x$ -MSE diagrams except the central sharp depression. It was concluded that the theoretical model of cardiac membrane excitation (hVC model) has only a single central sharp depression corresponding to the control model parameter.

277 Fig 1. Distribution of MSE calculated between the target and the simulated APs modified by randomizing the  $sf_x$  of 9 ionic  
 278 currents in the coordinates of MSE- $sf_x$ .  
 279 All MSE data points were plotted on the logarithmic ordinate against the linear  $sf_x$ . A total of 5,141,382 points were calculated in  
 280 cell model No.86 over the range of 1/10 ~ 10 times the default  $sf_x$ . Since the configuration of  $V_m$  records were largely unrealistic  
 281 at  $sf_x > 3$ , MSE points were cut out over  $sf_x > 3.0$ . To demonstrate the sharp decrease in MSE, the data points were densely  
 282 populated near the default  $sf_x$ .

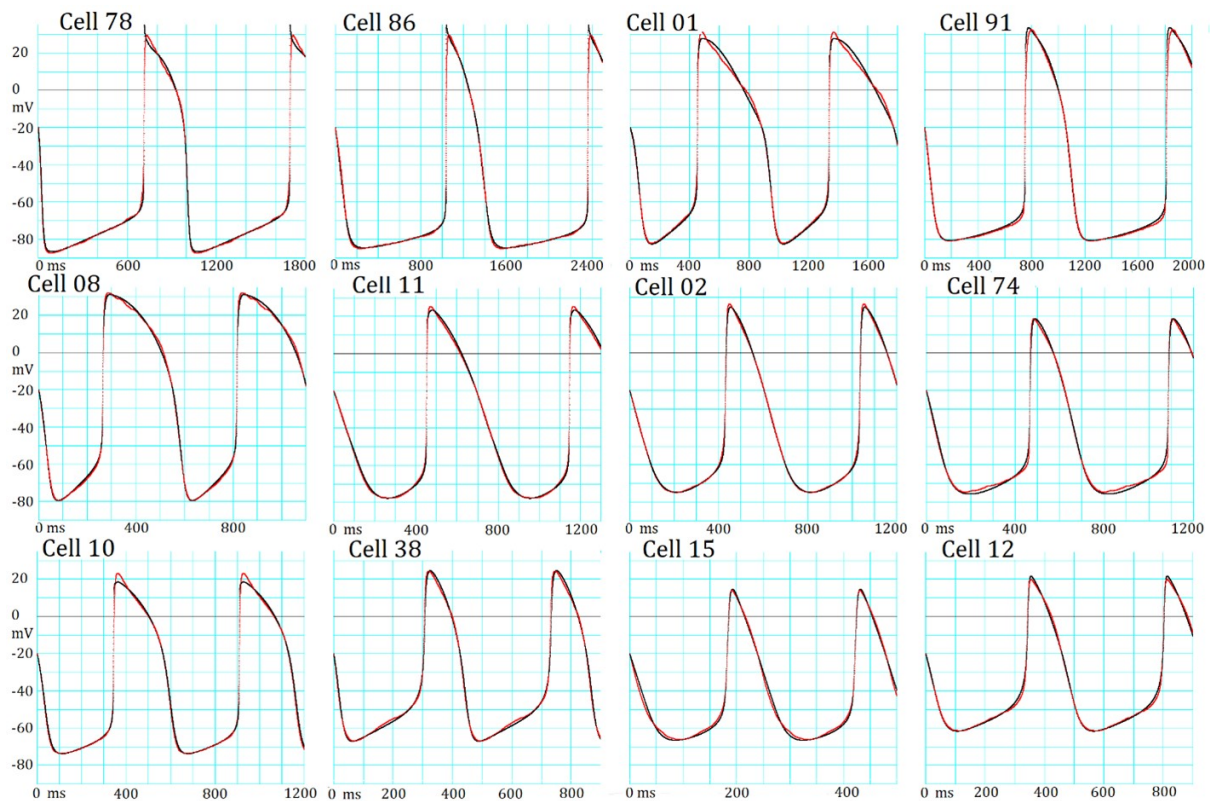
283

#### 284 4.2. The prompt necessity for a method of parameter optimization as indicated by hiPSC-CM APs

285 Fig 2 illustrates records of spontaneous APs (red traces) obtained in 12 experiments in the sequence of  
 286 MDP (See Supplemental Materials for detail). All experimental records were superimposed with the simulated  
 287 AP traces (black traces) obtained by the conventional manual fitting. In most cases, MSE of 1~6 mV<sup>2</sup>

288 remained (Eq 7) at the end of the manual fitting. This extra component of MSE might be largely attributed to  
 289 slow fluctuations of  $V_m$  of unknown origin in experimental recordings because the non-specific random  
 290 fluctuations were quite different from the exponential gating kinetics of ion channels calculated in  
 291 mathematical models. This extra-noise seriously interfered with the assessment of the accuracy of the  
 292 parameter optimization of  $G_x$  in the present study. Thus, APs produced by the manual adjustment ('cell  
 293 specific model') was used as the target AP, which were completely free from the extra noise when examining  
 294 the feasibility of the parameter optimization algorithm.

295 A comparison of AP configurations between these hiPSC-CMs clearly indicated that the classification  
 296 of these APs into atrial-, ventricular- and nodal-types was virtually impractical, as described in [7]. On the  
 297 other hand, if provided with the individual models fitted by an objective parameter optimizing tools using the  
 298 baseline model (black trace), the results should be fairly straightforward not only in estimating the functional  
 299 expression level of ion channels but also in clarifying the role of each current system or the ionic mechanisms  
 300 in generating the AP configuration in a quantitative manner. Thus, the objective parameter optimization of the  
 301 mathematical model is a vital requirement in cardiac electrophysiology.



302

303

304

305

306

307

308

Fig 2. The manual fitting of variable AP configurations in 12 different hiPSC-CMs. Each panel shows the experimental record (red) superimposed by the model output (black) of the baseline model adjusted by the conventional manual fitting. At the top of each pair of AP records, the experimental cell number is presented. The extra fluctuations are obvious during the AP plateau in Cells 78, 08 and 01, while in Cells 15 and 74 during SDD. The length of abscissa is markedly different to illustrate the interval between two successive peaks of AP.

309

310

311

Table 1. AP metrics and MSE calculated after the manual fitting of varying AP configurations in 12 different hiPSC-CMs in Fig 2.

312

313

314

315

Table 1 indicates the AP metrics; the cycle length (CL), the peak potential of the plateau (OS), the maximum diastolic potential (MDP), and the AP duration measured at -20 mV in addition to the MSE between individual experimental record and the model output fitted by manual fitting. The CL, MDP and AP were very variable among different AP recordings of cells shown in Fig 2. The cells were arranged by the sequence of MDP.

	CL (ms)	OS (mV)	MDP (ms)	APD(ms) at -20mV	MSE (mV <sup>2</sup> )
Cell 78	983.8	29.6	-87.4	271.7	5.8443
Cell 86	1326.0	29.7	-85.0	289.2	4.0554
Cell 01	887.4	31.2	-82.2	435.0	3.9330
Cell 91	1058.0	33.0	-80.4	308.6	7.2156
Cell 08	551.4	32.0	-79.5	287.6	1.4043
Cell 11	695.0	25.3	-77.6	243.5	2.6683
Cell 02	603.9	26.4	-74.9	173.4	1.0412
Cell 74	622.8	18.5	-74.8	157.0	2.2589
Cell 10	564.3	23.0	-73.7	220.9	3.2194
Cell 38	425.4	24.2	-66.8	123.4	3.6626
Cell 15	239.5	13.8	-66.1	57.1	2.8607
Cell 12	458.6	19.7	-61.5	119.0	1.3514

316

317

318

319

320

321

322

Table 1 indicates the AP metrics; the cycle length (CL), the peak potential of the plateau (OS), the maximum diastolic potential (MDP), and the AP duration measured at -20 mV in addition to the MSE between individual experimental record and the model output fitted by manual fitting. The CL, MDP and AP were very variable among different AP recordings of cells shown in Fig 2. The cells were arranged by the sequence of MDP.

323

**4.3. Feasibility of the PS algorithm for parameter optimization of membrane excitation models**

324

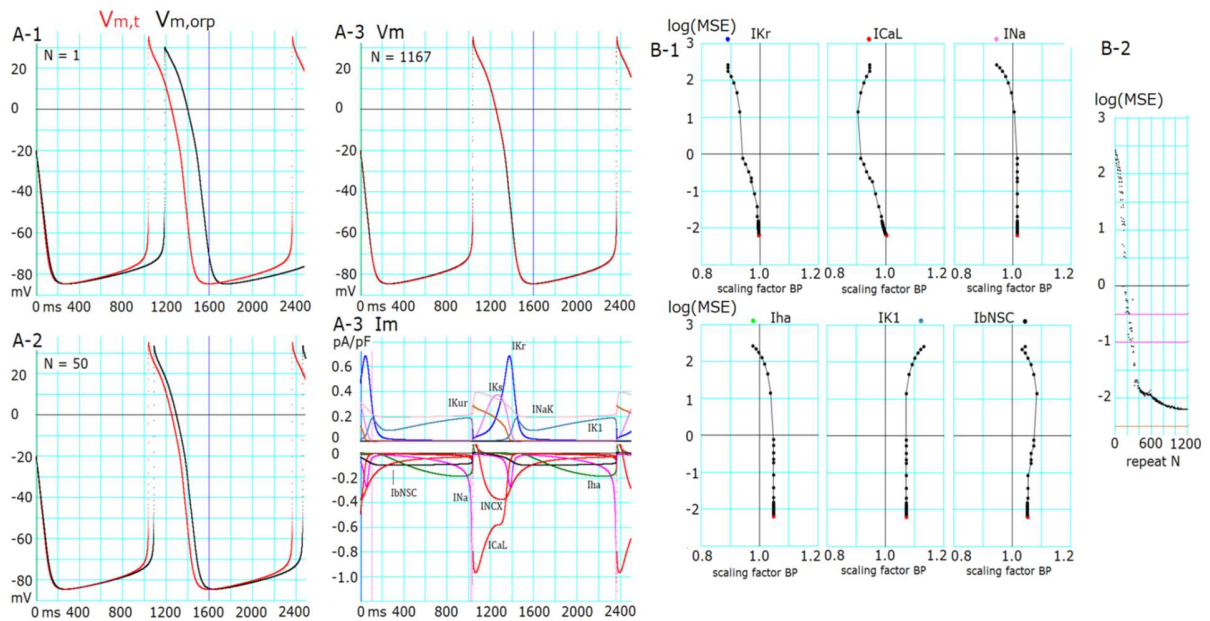
The automatic parameter optimization was applied to the model of cardiac membrane excitation in a limited

325

number of studies (for review, see [23,26,35,36]) using various optimization methods, such as genetic

326 algorithms. To the best of our knowledge, the principle PS algorithm has not been successfully applied to the  
 327 detailed mathematic models of cardiac membrane excitation composed of both ionic channel and ion  
 328 transporters models, except for the pioneering work in [12], which applied more general gradient-based  
 329 optimization method to the simple ventricular cell model of Beeler and Reuter (BR model)[37].

330 Fig 3 shows a typical successful run of the new PS method in a hiPSC-CM, which showed an MDP  
 331 of  $\sim -85$  mV. The PS parameter optimization was started after randomizing the  $sf_x$ s of the major six currents,  
 332  $I_{Kr}$ ,  $I_{CaL}$ ,  $I_{Na}$ ,  $I_{ha}$ ,  $I_{K1}$  and  $I_{bNSC}$ , in the manual fit model within a range of  $\pm 15\%$  around the default values  
 333 (normalized magnitude of 1). Fig 3A-1~3 compares the simulated  $V_{m,orp}$  (black) with the target  $V_{m,t}$  (red) at the  
 334 repeat number  $N=1, 50$  and  $1167$ , respectively (Eq 8). The OS, APD as well as the CL of spontaneous AP  
 335 were markedly different at the first cycle of AP reconstruction (Fig 3A-1). These deviations were largely  
 336 decreased at the PS cycle (Fig 3A-2  $V_m$ , at  $N = 50$ ), and became invisible in the final result (Fig 3A-3,  $N =$   
 337  $1167$ ). The final individual current flow of nine current components are demonstrated in the lower panel of  
 338 Fig 3A-3 ( $I_m$ ).



339  
 340 Fig 3. Results of the successful optimization in a cell (Cell86).  
 341 (A-1) Target AP ( $V_{m,t}$ , red) and AP generated by randomized initial  $sf_x$ s ( $V_{m,orp}$ , black). (A-2)  $V_{m,t}$  (red) and  $V_{m,orp}$  (black)  
 342 generated after 50 cycles of adjusting BP. (A-3)  $V_m$ :  $V_{m,t}$  (red) and  $V_{m,orp}$  (black) generated by the final  $sf_x$ s.  $I_m$ : corresponding  
 343 time courses of each current for the finalized AP shown in A-3  $V_m$ . (B-1) Changes in  $sf_x$ s vs.  $\log(\text{MSE})$  during a successful

344 optimization process of PS. (B-2)  $\log(MSE)$  of all BP points during the search process in PS. The initial values of  $sf_x$ s are  
345 plotted by corresponding colors at the top of each  $sf_x$ - $\log(MSE)$  graph.

346

347 The time course of decreasing  $\log(MSE)$  evoked by the multi-run PS optimization is plotted for each  
348  $sf_x$  in Fig 3B-1 every time of resetting the set of base points. Fig 3B-2 shows all of the  $\log(MSE)$  obtained at  
349 every adjustment by stepping individual BP points. The movement of all  $sf_x$ s were synchronized to decrease  
350  $\log(MSE)$  from  $\sim 2.4$  to 1 during the initial 180 cycles of decreasing  $\log(MSE)$ , but the search directions of  
351 BP were quite variable. The detailed adjustment of  $sf_x$ s below  $\log(MSE) < 0$  was driven by adjusting  $I_{Kr}$ ,  $I_{CaL}$   
352 and  $I_{bNSC}$  in this cell. The values of  $sf_{Kr}$ ,  $sf_{CaL}$  and  $sf_{Na}$  approached the correct value of 1, while those for  $I_{ha}$ ,  $I_{K1}$   
353 and  $I_{bNSC}$  remained deviated from the unit by less than 10% of the value. The explanation for the deviation of  
354 these three  $sf_x$ s from the unit will be examined in the next section of the Results.

355

356

#### 357 **4.4. The six-parameter orp test successfully determined the conductance parameters of membrane** 358 **excitation models**

359 In individual runs, the PS optimization was frequently interrupted at intermediate levels during the  
360 progress of optimization and the probability of reaching  $\log(MSE)$ , for example, below -2, rapidly decreased  
361 with increasing extent of the randomization of the initial set of parameters. Moreover, the complementary  
362 relations between several ionic currents in determining  $dV_m/dt$  might have hampered the parameter  
363 optimization. These facts indicate the requirement of statistical measures to improve the accuracy of the PS  
364 method. Fig 4 shows the results of orp tests, in which the optimization shown in Fig 3 was repeated several  
365 hundred times, and all results were plotted in a common coordinate of  $\log(MSE)$  and individual  $sf_x$ s. The  
366 population of  $sf_x$  correctly converged at a single peak point very close to 1 with increasing negativity of  
367  $\log(MSE)$  for  $sf_{Kr}$ ,  $sf_{CaL}$ , and  $sf_{Na}$ , while  $sf_{ha}$ ,  $sf_{K1}$ , and  $sf_{bNSC}$  showed obvious variance. Nevertheless, they also  
368 showed a clear trend toward convergence to 1 in the average.

369

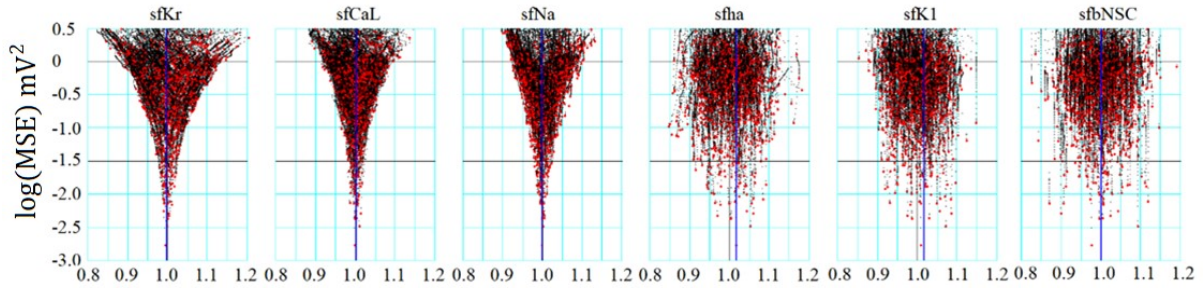


Fig 4. Convergence of  $sf_x$  in the orp test for Cell86. The ordinate is the  $\log(MSE)$  and the abscissa is the normalized amplitude of  $sf_x$ ;  $x$  stands for  $Kr$ ,  $CaL$ ,  $Na$ ,  $ha$ ,  $K1$ , and  $bNSC$ . Black points were obtained in the progress of optimization, and red ones are the final points in 829 runs of PS optimization.

370  
371  
372  
373

374

375 Table 2 summarizes the mean of  $sf_x$  determined for the top 20 runs of the PS parameter optimization in  
376 each of the 12 cells illustrated in Fig 2. The  $[Na^+]_i$  as well as  $Ca_{tot}$  was well controlled to the reference levels  
377 ( $std_{Na_i}$ , and  $std_{Ca_{tot}}$  in Eqs 16 and 17) of 6.1 mM and 79 amol, respectively, at the end of the parameter  
378 optimization to ensure the constant  $[Na^+]_i$  as well as  $Ca_{tot}$ . The mean of final  $\log(MSE) = -2.74$  indicates  
379 that the MSE was reduced by five orders of magnitude from the initial level just after the randomization by the  
380 orp test, like in the successful example shown in Fig 3B. The mean of individual  $sf_x$ s were very close to 1 with  
381 a minimum standard error (SE) of mean, which were less than 1% of the mean, even for  $I_{K1}$ ,  $I_{bNSC}$  and  $I_{ha}$ ,  
382 which showed weak convergence against  $\log(MSE)$ . These results well validate the accuracy of the parameter  
383 optimization using the multi-run PS method in all of 12 cell-specific models, which showed the large variety of  
384 spontaneous AP recorded in the hiPSC-CMs.

385

386 Table 2. Measurements of  $sf_x$ s (mean + SE,  $n = 20$ ),  $[Na^+]_i$ , mM and  $Ca_{tot}$  in amol in the 12 cells.

Cell No.	log(MSE)	sfKr	sfK1	sfCaL	sfbNSC	sfha	sfNa	sfKur	[Na <sup>+</sup> ] <sub>i</sub> (mM)	Ca <sub>tot</sub> (amol)
78	-2.48321	1.00005	1.00157	1.00037	0.99460	1.00060	1.00134		6.10550	78.99979
91	-2.42008	0.99952	1.00644	1.00063	1.00280	1.00470	1.00068		6.09977	79.00044
86	-2.80257	1.00166	1.01394	1.00142	1.02670	1.00253	1.00702		6.09466	79.00008
01	-2.79709	0.99871	1.00157	0.99756	0.99692	1.00054	0.99779		6.08973	78.99984
08	-3.07432	0.00094	0.99982	1.00088	1.00041	0.99968	0.99985		6.12201	79.00056
11	-2.67641	1.00186	1.00686	1.00129	0.99768	1.00253	1.01028		6.10385	78.99995
10	-1.70278	1.00322	1.01081	1.00424	1.00396		0.99883		6.10968	79.00018
02	-2.35441	1.00161	1.02038	1.00341	0.99815	1.01324	1.00954		6.10184	79.00004
74	-2.43399	1.00126	1.01838	1.00308	0.99898	1.00004	1.00435		6.10118	79.99979
38	-3.01883	1.00075		1.00106	1.00061		0.98866	1.00151	6.10530	78.99969
15	-3.85992	1.00003		0.99894	0.99996		1.00015	0.98653	6.09902	79.00022
12	-3.33037	0.99978		1.00030	0.99990	0.97587		1.00188	6.10012	79.00007
Ave	-2.74617	0.99992	1.00886	1.00110	1.001723	0.99997	1.001681	0.99664	6.10272	79.08339
SE	0.07065	0.00093	0.010000	0.00164	0.00430	0.00729	0.00544	0.00690	0.00017	0.000345

387 The top 20 results obtained in the multi-run orp method were analyzed in each cell. Grand average (Ave) and  
 388 SE are listed at the bottom rows.

389

390 **4.5. Complementary relationship among  $I_{K1}$ ,  $I_{ha}$  and  $I_{bNSC}$**

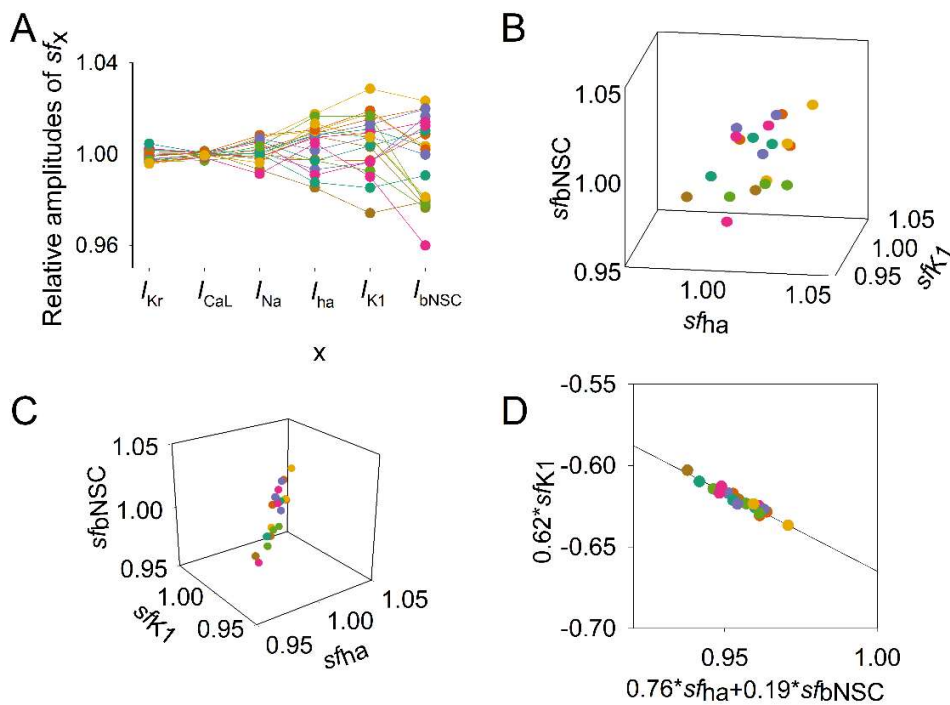
391 Fig 5A illustrates the distribution of  $sf_x$ s amplitude in the top 20 data points, where the final  $sf_x$ s in  
 392 individual runs were connected with lines for each run of PS in Cell 86 (Fig 2). The values of standard error  
 393 (SE) of mean were quite small in the  $sf_{Kr}$  and  $sf_{CaL}$ , less than 1%. In contrast,  $sf_{ha}$ ,  $sf_{K1}$  and  $sf_{bNSC}$  showed  
 394 evidently larger deviations. This finding is interesting since the former currents are mainly involved in  
 395 determining the AP configuration and the latter group mainly in driving the relatively long-lasting SDD of  
 396 approximately 1 sec in duration.

397 Thus, we analyzed the distribution of  $sf_{ha}$ ,  $sf_{K1}$  and  $sf_{bNSC}$  within the top 20 MSE. Fig 5B and C show  
 398 the distribution of  $sf_x$  points in the space of the three  $sf_x$  dimensions. In Fig 5B, the 20 data points seemed to be  
 399 dispersed randomly in the parameter space, but when the space was rotated to a specific angle, a linear  
 400 distribution was observed as in Fig 5C, indicating that the points are distributed approximately on a plane  
 401 surface in the 3D space. Using the multiple regression analysis, we could obtain an equation that fits the 20  
 402 data points as follows ( $R^2=0.872$ );

403 
$$0.762 \cdot sf_{ha} - 0.619 \cdot sf_{K1} + 0.191 \cdot sf_{bNSC} = 0.333554$$
 Eq 16

404  
405  
406  
407  
408  
409  
410

By replotting the data points in the 2D space with the abscissa for the sum of two inward-going currents ( $0.76 sf_{ha} + 0.19 sf_{bNSC}$ ) and the ordinate for the outward current  $0.62 sf_{K1}$ , we obtained a regression line as shown in Fig 5D. The close correlations among the three  $sf_x$ s were indicated with a quite large  $R^2$  of 0.941. This finding well confirms that the three currents have complementary relations with each other to give virtually identical configurations of spontaneous AP. In other words,  $\log(MSE)$  remains nearly constant as far as the composition of the currents satisfies the relationship given by Eq 16.



411  
412  
413  
414  
415  
416

Fig 5. Distribution of  $sf_x$  within the top 20 sets of  $sf_x$ S obtained from the multi-run orp test in Cell86 in Fig 2. Data points of normalized  $sf_x$  in each set were depicted in a different color. (A) amplitudes of each  $sf_x$  (indicated on the abscissa) were plotted. (B) Three parameters,  $sf_{ha}$ ,  $sf_{K1}$ , and  $sf_{bNSC}$  were plotted in the 3D plot. (C) A different solid angle view of the 3D plot showed a linear correlation; see text for the plot in (D)

417  
418  
419  
420  
421

The complementary relationship was further examined by conducting the orp test after fixing one of the two factors,  $sf_{K1}$  or  $(sf_{ha} + sf_{bNSC})$ , illustrated in Fig 5B. Fig 6A shows the  $\log(MSE)$  vs.  $sf_{K1}$  relation when the  $(sf_{ha} + sf_{bNSC})$  were fixed at the values obtained by the orp test. Indeed, the typical convergence of the  $sf_{K1}$  was obtained. Alternatively, if the  $sf_{K1}$  was fixed, the convergence was obviously improved for both  $sf_{ha}$  and  $sf_{bNSC}$  (Fig 6B-1, 2), but it was less sharp if compared to  $sf_{Kr}$ ,  $sf_{CaL}$  and  $sf_{Na}$  (not shown, but refer to

422 corresponding results in Fig 4A). This finding was further explained by plotting the relationship between the  
 423 two inward currents,  $I_{ha}$  and  $I_{bNSC}$ , as illustrated in Fig 6C. The regression line for the data points was fitted by  
 424 Eq 17 with  $R^2 = 0.86$ , supporting the complementary relationship between the two inward currents,  $I_{ha}$  and  $I_{bNSC}$ .

$$425 \quad 0.9736 \cdot sf_{bNSC} + 0.2281 \cdot sf_{ha} = 1.2024 \quad Eq\ 17$$

426

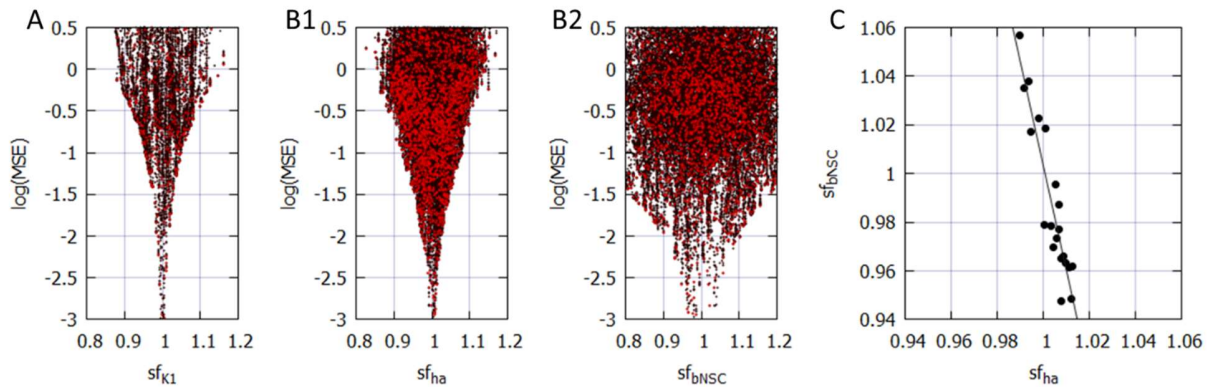
427 The moderately high  $R^2$  indicates that the SDD is determined not only by the major  $I_{ha}$  and  $I_{bNSC}$  but  
 428 also by other currents, such as  $I_{K1}$ ,  $I_{Kr}$ , the delayed component of  $I_{Na}$  ( $I_{NaL}$ ) and  $I_{CaL}$ , which were recorded  
 429 during the SDD as demonstrated in Fig 3.

430 Essentially the same results of complementary relationship among  $sf_{ha}$ ,  $sf_{bNSC}$  and  $sf_{K1}$  were obtained in  
 431 Cell 91, which also showed the long-lasting SDD with the very negative MDP as in Cell 86, as shown in Fig 2  
 432 and Table 2. The regression relation for the data points was fitted by Eqs 18 and 19 with  $R^2 = 0.656$  and  
 433 0.472, respectively.

$$434 \quad 0.572 \cdot sf_{ha} - 0.132 \cdot sf_{K1} + 0.810 \cdot sf_{bNSC} = 1.25891 \quad Eq\ 18$$

$$435 \quad 0.9279 \cdot sf_{ha} + 0.3706 \cdot sf_{bNSC} = 1.30025 \quad Eq\ 19$$

436

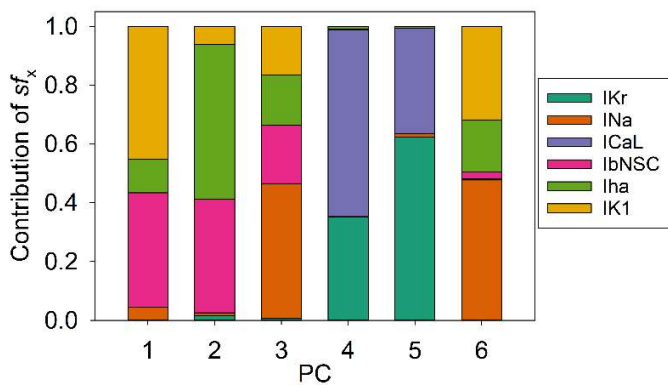


437 Fig 6. The complementary relations among  $sf_{K1}$ ,  $sf_{ha}$  and  $sf_{bNSC}$ .  
 438 (A) and (B) results of the multi-run orp test. A; the perfect convergence of  $sf_{K1}$  when  $sf_{ha}$  and  $sf_{bNSC}$  were fixed. (B1) improved  
 439 convergence of  $sf_{ha}$  and (B2)  $sf_{bNSC}$  when  $sf_{K1}$  was fixed. In these two orp tests,  $sf_x$  of other currents showed quite comparable  
 440 convergence as in Fig 4A. (C) the correlation between  $sf_{ha}$  and  $sf_{bNSC}$ .  
 441

## 442 4.6. Principal components in the hiPSC-CM model

443 The PS frequently got stuck during the progress of parameter optimization and failed to reach the  
 444 global minimum in the present study (Figs 4 and 6). The major cause of this interruption may most probably be  
 445 attributed to the fact that  $sf_x$ s were used directly as the search vector of the PS. In principle, the algorithm of PS  
 446 parameter optimization gives the best performance when the parameters search is conducted in orthogonal  
 447 dimensions where each dimension does not affect the adjustment of other  $sf_x$  [28]. To get deeper insights, we  
 448 applied the principal component (PC) analysis to the set of 6  $sf_x$ s selected in the baseline model. We performed  
 449 PC analysis on the data points recorded in the vicinity of the minima (using the top 20 data).

450 As illustrated in Fig 7, each of the 6 PCs was not composed of a single  $sf_x$  but mostly included  
 451 multiple  $sf_x$  sub-components. This finding indicates the inter-parameter interactions during the process of  
 452 parameter optimization. For example, the changes in  $sf_{K1}$  or  $sf_{bNSC}$  simultaneously affect PCNo.1, 3, 6 or 1, 2, 3  
 453 PCs, respectively. Both  $sf_{CaL}$  and  $sf_{Kr}$  affect PCNo.4, 5. It might be concluded that the frequent interruptions of  
 454 PS parameter optimization are most probably caused by the sporadic appearance of the local minima of MSE  
 455 through interactions among  $sf_x$ s.



456

457 Fig 7. PC1~6 to describe distribution of the 6  $sf_x$ s. PC analysis was performed on the data population of the top 200 runs of the  
 458 orp test as in Fig 4, which showed good optimization results (Cell 86). Each magnitude of 6 PCs was normalized to give a unit  
 459 magnitude. Note each PC is composed of multiple components of ionic current, which are indicated in the Index with  
 460 corresponding colors.

461

462

463

464 5. Discussion

465 New findings in the present study are listed below.

- 466 (1) Mapping the MSE distribution over the enlarged parameter space was conducted by randomizing  
467 the  $G_{xS}$  of the baseline model. It was confirmed that the baseline model has only a single sharp  
468 depression of MSE at the default  $G_{xS}$  (Fig 1).
- 469 (2) The preliminary cell-specific models were firstly prepared by the conventional manual tuning of  
470  $G_{xS}$  to superimpose the model output on each of twelve experimental AP recordings (Fig 2).  
471 Thereby, the parameter search space was restricted to a relatively small space to facilitate  
472 parameter optimization.
- 473 (3) The  $sf_{xS}$  of 4 ~ 6  $G_x$  parameters were initially assigned random values from a uniform distribution  
474 ranging between  $\pm 10\%$  of default values. The MSE was calculated between the randomized  
475 model output and the intact model AP as the target of optimization (Fig 3).
- 476 (4) Plotting parameter  $sf_x$  in a common  $sf_x$  - MSE coordinates during each run of several hundred runs  
477 of optimization (Fig 4), we found that the  $sf_x$  distribution of  $I_{Kr}$ ,  $I_{CaL}$ , and  $I_{Na}$  converged sharply to  
478 a single point with decreasing MSE, which exactly equaled the default ones. On the other hand,  
479 estimates of  $sf_{K1}$ ,  $sf_{ha}$  and  $sf_{bNSC}$  deviated slightly within a limited range around the default values  
480 in cells showing long-lasting SDD (Fig 4).
- 481 (5) For statistical evaluation, the mean  $\pm$  SE of  $sf_x$  in the top 20 estimates of MSE was calculated in  
482 individual cells (Table 2). The results of the parameter optimization in the 12 cells definitely  
483 indicated that the means of  $sf_{xS}$  were very close to 1.00, with the SE less than 0.01 for all  $G_{xS}$ .
- 484 (6) A complementary relationship was found between  $sf_{K1}$ ,  $sf_{ha}$  and  $sf_{bNSC}$  in determining the gentle  
485 slope of long-lasting SDD in two representative cells (Fig 5). Supporting this view, the  $sf_{K1}$  clearly  
486 focused on the unit provided that  $sf_{ha}$  and  $sf_{bNSC}$  were fixed and vice versa (Fig 6).
- 487 (7) The six search vectors of  $sf_x$  of the presented model could be replaced by the same number of  
488 theoretical PCs, and each PC was mostly composed of multiple  $sf_{xS}$  (Fig 7). This finding  
489 definitely supports the view [12] that the complex interactions among  $I_{xS}$  might interrupt the

490 progress of the parameter optimization when  $sf_x$ s were used as the search vector instead of using  
491 theoretical orthogonal ones.

492

493 The use of an initial randomized set of parameters was crucial in examining if an optimization method  
494 can determine unique estimates independent from the initial set of parameters, as used in the GA-based method  
495 for determining the  $G_x$ s of the mathematical cardiac cell model [23]. The findings listed above well confirmed  
496 the feasibility of the PS method. Most probably, the PS method is applicable to variable mathematical models  
497 of other cell functions as well. See [26] for a more systematic review of the parameter optimization in the  
498 cardiac model development.

499 It has been suggested that different combinations of parameters may generate simple outputs that are  
500 very similar [12,23–25]. In the present study, this notion may be explained at least in part by the  
501 complementary relationship, for example, between the  $I_{K1}$ ,  $I_{ha}$  and  $I_{bNSC}$  in determining  $dV_m/dt$  of SDD, which  
502 is a function of the total current (Eq 2, Figs 5 and 6). The gradient-based optimization method relies on the  
503 precise variation in the time course of  $dV_m/dt$  induced by the time-dependent changes in individual  $sf_x$ s (Eq 2).  
504 Therefore, the MSE was calculated over the whole time course of the spontaneous APs. Note, we did not use  
505 the AP metrics, which reflect only indirectly the kinetic properties of individual currents. Even with this  
506 measure of calculating the MSE, the time-dependent changes in  $pO$  (Eq 3) might be relatively small between  
507 two major currents,  $I_{K1}$  and  $I_{ha}$ , in comparison to  $I_{bNSC}$ , which has no  $V_m$ -dependent gate during the SDD as  
508 shown in the current profile Fig 3A-3. We assume that the gradient-based optimization method will be able to  
509 determine different contributions of individual currents if the optimization is conducted only within a selected  
510 time window of SDD. If MSE is calculated over multiple phases of the spontaneous AP, the influence of a  
511 particular phase on the MSE should be diluted. In our preliminary parameter optimization, this problem was  
512 partly solved by using a weighted sum for different phases of the spontaneous AP in summing up the MSE.

513 The small amplitude of a given current might be an additional factor in the weak convergence of  $sf_x$   
514 observed in the diagram of  $sf_x$  - MSE in the orp test of optimization. If the current amplitude was much  
515 smaller in reference to the sum of all currents in determining  $dV_m/dt$  (Eq 2), the resolution of the PS method  
516 would get lower. Sarkar et al. [24] demonstrated that the model output, for example, the AP plateau phase were

517 almost superimposable when the different ratio of  $G_{Kr}$  and  $G_{pK}$  were used in reconstructing the model output  
518 (Figure 1 in [24]). They described that the AP metrics used for comparisons, such as APD, OS and APA  
519 seemed quite similar. It should be noted, however, that the results were obtained by applying different  
520 combinations of  $sf_x$  to the same TNNP model [33]. This means that the relative amplitudes of  $I_{Kr}$  and  $I_{pK}$  in the  
521 TNNP model were much smaller than the major  $I_{CaL}$  during the AP plateau, even though  $I_{Kr}$  and  $I_{pK}$  have  
522 totally different gating kinetics. Thus, the results of parameter optimization should be model-dependent. The  
523 same arguments will also be applied to the use of FR guinea pig model [38] in the study by Groenendaal et al.  
524 [23].

525         The gradient-based parameter optimization method was applied to the cardiac model of membrane  
526 excitation in [12], which analyzed the classic BR model [37]. The whole cell current in the BR model was  
527 composed of a minimum number of ionic currents, a background  $I_{K1}$ , and three time-dependent currents;  $I_{Na}$ ,  $I_s$ ,  
528 and  $I_{K1}$ , which were dissected from the voltage clamp experiments by applying the sucrose gap method to the  
529 multicellular preparation of ventricular tissue. The gatings of the latter three currents were formulated  
530 according to the Hodgkin-Huxley type gating kinetics, which was quite simple if compared with the recent  
531 detailed description of the ionic currents. They described that the parameter optimization was difficult if the  
532 AP configuration was used as the target of the parameter optimization, and they used the time course of the  
533 whole cell current as of the target of parameter optimization. However, the number of parameters was quite  
534 large, 63 in total, including limiting conductances and the gating kinetics. They suggested the feasibility of the  
535 parameter optimization method will be improved if provided with additional experimental data.

536         In the modern mathematical cardiac cell models, most ionic currents were identified by the whole-cell  
537 voltage clamp and single channel recordings in dissociated single myocyte [39] using the patch clamp  
538 technique [40] and by identifying their molecular basis of membrane protein. It has been clarified that the  
539 molecular basis of the ion channels expressed in the hiPSC-CMs is mostly identical to those in the adult  
540 cardiac myocytes rather than in the fetal heart (GSE154580 GEO Accession viewer (nih.gov)). Moreover, the  
541 gating kinetics have been much detailed to characterize the ionic currents within the cell model. In principle,  
542 the detailed characterization of individual currents should facilitate the identifiability of the model parameter  
543 but should not necessarily interfere with parameter optimization. We consider that the manual fitting of the

544 model parameters to the AP recording by using a priori knowledge of biophysical mechanisms should largely  
545 facilitate the subsequent automatic parameter optimization. It might also be noted that the ionic currents left at  
546 the default values work as a kind of constraint to improve the identifiability of the target parameters.

547         After validating the automatic parameter optimization method, the final goal of our study is to find the  
548 principle of ionic mechanisms, which are applicable to the full range of variations of spontaneous AP records  
549 in both hiPSC-CMs and matured cardiomyocytes. For this purpose, we will apply the multi-run PS method to  
550 the experimental AP recordings using the initial parameter sets obtained by the conventional manual fit. The  
551 protocol of measuring the  $G_x$ s will be the same as used in the present study except for the use of experimental  
552 AP recordings in place of the output of the 'cell-specific model'. In our preliminary analysis, the magnitude of  
553 individual model parameters obtained by the manual tuning was corrected by less than  $\sim 15\%$  by the objective  
554 parameter optimization. Finally, the ionic mechanisms underlying the SDD of variable time courses will be  
555 analyzed in a quantitative manner, for example, by using the lead potential analysis [41], which explains  
556 changes in  $V_m$  in terms of  $G_x$  of individual currents.

557

## 558 **Limitations**

559         In general, obvious limitations of the mathematical models of cardiac membrane excitation so far  
560 published are caused by a shortage of functional components inherent in intact cells. For example, the  $[ATP]_i$   
561 controlled by energy metabolism is a vital factor in maintaining the physiological function of ion channels as  
562 well as the active transport  $Na^+/K^+$  pump [42]. Moreover, the followings are still not implemented in most  
563 models; the modulation of the ion channel activity through phosphorylation of the channel proteins, detailed  
564 modulation of the channel by the  $[Ca^{2+}]_i$ , the alterations of ion channel activity by  $PIP_2$  [43,44] and by the  
565 tension of the cell membrane through the cell volume change [45–48]. The detailed  $Ca^{2+}$  dynamics of the  
566  $[Ca^{2+}]_i$  are still not implemented in most of the cardiac cell models; such as the  $Ca^{2+}$  release from SR activated  
567 through the coupling of a few L-type  $Ca^{2+}$  channels with a cluster of RyRs at the dyadic junction [49], the  $Ca^{2+}$   
568 diffusion influenced by the  $Ca^{2+}$ -binding proteins [50]. To simulate the  $Ca^{2+}$ -binding to troponin during the  
569 development of the contraction, it is necessary to include a dynamic model of contracting fibers [51–54].

570 These limitations should be thoroughly considered when pathophysiological phenomena, such as  
571 arrhythmogenesis are concerned. The scope of the present study is limited to the AP configurations of hiPSC-  
572 CMs, which were assumed to be 'healthy' with respect to the above concerns; for example,  $[ATP]_i$ ,  $[Na^+]_i$  and  
573  $Ca_{tot}$  were kept constant, and the standard contraction model was implemented as in the hVC model.

574 The parameter optimization presented in this study could be achieved in a practical way by limiting  
575 the number of unknown parameters. We determined only  $G_{xS}$  based on the assumption that ion channel  
576 kinetics are preserved as the same in the hiPSC-CMs as in the matured myocytes. Usually, 4~6 ionic currents  
577 were selected for the optimization. We found that the orp method could be performed simultaneously for all  
578 nine ionic currents described in Eq 1. However, the computation time was radically prolonged, and the  
579 resolution was not as high as obtained by using the modest number of parameters. We consider that the  
580 determination of the limited number of  $G_{xS}$  is quite relevant to solving physiological problems in terms of  
581 detailed model equations for each current system.

582

583 Although  $I_{NCX}$  and  $I_{NaK}$  contribute sizeable fractions of the whole-cell outward and inward currents,  
584 respectively (Fig 3A-3), we excluded the scaling factors,  $sf_{NaK}$  and  $sf_{NCX}$  from the parameter optimization for  
585 the sake of simplicity. Instead, the possible drift of the intracellular ion concentrations was virtually fixed  
586 during the repetitive adjustment of ionic fluxes by varying  $sf_x$  as shown in Table 2. The introduction of the  
587 empirical equations (Eqs 13 and 14) was quite useful to adjust the  $[Na^+]_i$  and  $Ca_{tot}$  (Table 2) so that the time  
588 course as well as magnitude of  $I_{NCX}$  remained almost constant during the parameter optimization. When  
589 influences of varying  $[Na^+]_i$  and/or  $Ca_{tot}$  are examined under various experimental conditions in future, the  
590 reference levels of  $[Na^+]_i$  and/or  $Ca_{tot}$  ( $stdNai$  and  $stdCatot$  in Eqs 13 and 14) might be replaced by  
591 experimental measurements.

592 The parameter optimization method was not applied to several ionic currents. For example, it was  
593 difficult to determine the kinetics of T-type  $Ca^{2+}$  channel ( $I_{CaT}$ ; Cav 3.1) and excluded in the present study. A  
594 very fast opening and inactivation rates described in [55] suggest a complete inactivation of  $I_{CaT}$  over the  
595 voltage range of SDD, while a sizeable magnitude of window current described in [56] suggests a much larger  
596 contribution to SDD. The kinetics of  $I_{CaT}$  still remain to be clarified in experimental examinations. The

597 sustained inward current,  $I_{st}$ , is recently attributed most probably to the Cav 1.3 [57], which is activated at a  
598 more negative potential range than the activation of  $I_{CaL}$  (Cav 1.2) [58,59]. The  $I_{bNSC}$  was used to represent net  
599 background conductance in the present study. However, several components of the background conductance  
600 have been identified on the level of molecular basis in matured myocytes (see for review TRPM4, [60]).  
601 Experimental measurements of the current magnitude for each component are also awaited.

602 Gábor and Banga indicated that the multi-run method had shown good performance in certain cases,  
603 especially when high-quality first-order information is used and the parameter search space is restricted to a  
604 relatively small domain [16] (see also [19]). Indeed, the manual fitting of the parameters (Fig 1) was required  
605 to utilize the presented multi-run PS method over the restricted search space. One of the major difficulties in  
606 the manual fitting of individual  $G_x$ s arose during the SDD, where  $I_{Kr}$ ,  $I_{K1}$ ,  $I_{bNSC}$ , and  $I_{ha}$ , in addition to  $I_{NaK}$  and  
607  $I_{NCX}$  constitute the whole-cell current (Fig 3A-3). Close inspection of the current components (Fig 3A-3),  
608 however, suggests hints of how to do with the manual fit. The transient peak of  $I_{Kr}$  dominates the current  
609 profile during the final repolarization phase from -20 to -60 mV in all 12 hiPSC-CMs [61], since  $I_{CaL}$  and  $I_{Ks}$   
610 rapidly deactivated before repolarizing to this voltage range. The  $I_{NaK}$  and  $I_{NCX}$  are well controlled by the  
611 extrinsic regulation in Eqs 13 and 14. Thus, the manual fitting of  $sf_{Kr}$  is firstly applied to determine  $sf_{Kr}$ . The  
612 MDP more negative than -70 mV is adjusted by the sum of time-dependent ( $I_{Kr} + I_{K1}$ ) and the time-  
613 independent  $I_{bNSC}$ . Then,  $I_{Kr}$  is deactivated when depolarization becomes obvious after the MDP, and gradual  
614 activation of  $I_{ha}$  and the depolarization-dependent blocking of  $I_{K1}$  by the intracellular substances [62] take the  
615 major role in promoting the initial linear phase of SDD. Thus, the amplitude of  $sf_{K1}$  and  $sf_{bNSC}$  might be  
616 approximated during the initial half of SDD. The late half of SDD, including the foot of AP, namely the  
617 exponential time course of depolarization toward the rapid rising phase of AP, is mainly determined by the  
618 subthreshold  $V_m$ -dependent activation of  $I_{Na}$  (after MDP more negative than -70 mV) and/or  $I_{CaL}$  (after MDP  
619 less negative than -65 mV). Thus, the  $sf_{Na}$  and  $sf_{CaL}$  are roughly determined by fitting the foot of AP and the  
620 timing of the rapid rising phase of AP. The plateau time course of AP is determined by  $sf_{CaL}$  and the factor of  
621  $Ca^{2+}$ -mediated inactivation of  $I_{CaL}$  (the parameter  $KL$ , [4]). Since the kinetics of outward currents,  $I_{Kw}$ ,  $I_{Kto}$   
622 (*endo-type*), and  $I_{Ks}$  are quite different from that of  $I_{Kr}$ , the plateau configuration is determined bit by bit by

623 adjusting these currents. We failed to observe the phase 1 rapid and transient repolarization in the hiPSC-CMs  
624 (Fig 2), which is the typical sign of the absence of epicardial-type  $I_{Kto}$ .

625 In hiPSC-CMs showing less negative MDP than  $\sim -65$  mV, the contribution of  $I_{K1}$ ,  $I_{Na}$  and  $I_{ha}$  should  
626 be negligibly small because  $I_{K1}$  is nearly completely blocked by the intracellular  $Mg^{2+}$  and polyamine,  $I_{Na}$  is  
627 inactivated, and  $I_{ha}$  is deactivated during SDD, even if any expressed.

628 Nevertheless, parameter optimization might be laborious and time-consuming for those who are not  
629 familiar with the electrophysiology of the cardiac myocyte. This difficulty might be largely eased by  
630 accumulating both AP configurations and the underlying current profile obtained in the parameter optimization  
631 into a database in the future. If this database becomes available, the computer may search for several candidate  
632 APs for the initial parameter set, which is used for automatic parameter optimization.

633

## 634 **6. Funding and financial conflicts of interest**

635 The authors declare that the research was conducted without any commercial or financial relationships  
636 that could be construed as a potential conflict of interest.

637 This work was supported by JSPS KAKENHI (Grant-in-Aid for Young Scientists) Grant Numbers  
638 JP19K17560 for HK, 16K18996 for YH, and 21K06781 for FT.

639

## 640 **7. Author Contributions**

641 HK, YH, DY, YW, AK, and TM performed the wet experiments and analyzed them. HK, SK, YH,  
642 YZ, FT, AA, and AN developed the simulation model and the parameter optimization method. HK, YH, AA  
643 and AN wrote the manuscript. All authors reviewed the manuscript. AA and TK organized the research team.

644

## 645 **8. Acknowledgments**

646 The authors would like to thank our laboratory colleagues for their valuable comments and  
647 discussions.

648 **9. Data availability**

649 AP records used in section 4.2, and source code of the optimization program are available in the  
650 Supplemental Material link of the following bioRxiv entry.

651 <https://doi.org/10.1101/2022.05.16.492203>

652

653

654 **10. References**

655

656 1. Noble D, Garny A, Noble PJ. How the Hodgkin-Huxley equations inspired the Cardiac Physiome Project:  
657 Hodgkin-Huxley equations and the cardiac Physiome Project. *J Physiology*. 2012;590: 2613–2628.  
658 doi:10.1113/jphysiol.2011.224238

659 2. Noble D, Rudy Y. Models of cardiac ventricular action potentials: iterative interaction between experiment  
660 and simulation. *Philosophical Transactions Royal Soc Lond Ser Math Phys Eng Sci*. 2001;359: 1127–1142.  
661 doi:10.1098/rsta.2001.0820

662 3. Winslow RL, Cortassa S, O'Rourke B, Hashambhoy YL, Rice JJ, Greenstein JL. Integrative modeling of the  
663 cardiac ventricular myocyte. *Wiley Interdiscip Rev Syst Biology Medicine*. 2011;3: 392–413.  
664 doi:10.1002/wsbm.122

665 4. Hinch R, Greenstein JL, Tanskanen AJ, Xu L, Winslow RL. A Simplified Local Control Model of Calcium-  
666 Induced Calcium Release in Cardiac Ventricular Myocytes. *Biophys J*. 2004;87: 3723–3736.  
667 doi:10.1529/biophysj.104.049973

668 5. Paci M, Hyttinen J, Aalto-Setälä K, Severi S. Computational models of ventricular- and atrial-like human  
669 induced pluripotent stem cell derived cardiomyocytes. *Ann Biomed Eng*. 2013;41: 2334–2348.  
670 doi:10.1007/s10439-013-0833-3

671 6. Paci M, Hyttinen J, Rodriguez B, Severi S. Human induced pluripotent stem cell-derived versus adult  
672 cardiomyocytes: an in silico electrophysiological study on effects of ionic current block. *Brit J Pharmacol*.  
673 2015;172: 5147–5160. doi:10.1111/bph.13282

674 7. Lei CL, Wang K, Clerx M, Johnstone RH, Hortigon-Vinagre MP, Zamora V, et al. Tailoring Mathematical  
675 Models to Stem-Cell Derived Cardiomyocyte Lines Can Improve Predictions of Drug-Induced Changes to  
676 Their Electrophysiology. *Front Physiol*. 2017;8: 986. doi:10.3389/fphys.2017.00986

677 8. Grandi E, Pasqualini FS, Bers DM. A novel computational model of the human ventricular action potential  
678 and Ca transient. *Journal of molecular and cellular cardiology*. 2010;48: 112–121.  
679 doi:10.1016/j.yjmcc.2009.09.019

- 680 9. O'Hara T, Virág L, Varró A, Rudy Y. Simulation of the Undiseased Human Cardiac Ventricular Action  
681 Potential: Model Formulation and Experimental Validation. McCulloch AD, editor. *Plos Comput Biol.* 2011;7:  
682 e1002061-29. doi:10.1371/journal.pcbi.1002061
- 683 10. Asakura K, Cha CY, Yamaoka H, Horikawa Y, Memida H, Powell T, et al. EAD and DAD mechanisms  
684 analyzed by developing a new human ventricular cell model. *Prog Biophysics Mol Biology.* 2014;116: 11–24.  
685 doi:10.1016/j.pbiomolbio.2014.08.008
- 686 11. Himeno Y, Asakura K, Cha CY, Memida H, Powell T, Amano A, et al. A Human Ventricular Myocyte  
687 Model with a Refined Representation of Excitation-Contraction Coupling. *Biophys J.* 2015;109: 415–427.  
688 doi:10.1016/j.bpj.2015.06.017
- 689 12. Dokos S, Lovell NH. Parameter estimation in cardiac ionic models. *Prog Biophysics Mol Biology.*  
690 2004;85: 407–431. doi:10.1016/j.pbiomolbio.2004.02.002
- 691 13. Dutta S, Chang KC, Beattie KA, Sheng J, Tran PN, Wu WW, et al. Optimization of an In silico Cardiac  
692 Cell Model for Proarrhythmia Risk Assessment. *Front Physiol.* 2017;8: 616. doi:10.3389/fphys.2017.00616
- 693 14. Whittaker DG, Clerx M, Lei CL, Christini DJ, Mirams GR. Calibration of ionic and cellular cardiac  
694 electrophysiology models. *Wiley Interdiscip Rev Syst Biology Medicine.* 2020;12: e1482.  
695 doi:10.1002/wsbm.1482
- 696 15. Cairns DI, Fenton FH, Cherry EM. Efficient parameterization of cardiac action potential models using a  
697 genetic algorithm. *Chaos Interdiscip J Nonlinear Sci.* 2017;27: 093922. doi:10.1063/1.5000354
- 698 16. Gábor A, Banga JR. Robust and efficient parameter estimation in dynamic models of biological systems.  
699 *Bmc Syst Biol.* 2015;9: 74. doi:10.1186/s12918-015-0219-2
- 700 17. Degasperi A, Fey D, Kholodenko BN. Performance of objective functions and optimisation procedures for  
701 parameter estimation in system biology models. *Npj Syst Biology Appl.* 2017;3: 20. doi:10.1038/s41540-017-  
702 0023-2
- 703 18. Penas DR, González P, Egea JA, Doallo R, Banga JR. Parameter estimation in large-scale systems biology  
704 models: a parallel and self-adaptive cooperative strategy. *Bmc Bioinformatics.* 2017;18: 52.  
705 doi:10.1186/s12859-016-1452-4
- 706 19. Villaverde AF, Fröhlich F, Weindl D, Hasenauer J, Banga JR. Benchmarking optimization methods for  
707 parameter estimation in large kinetic models. *Bioinformatics.* 2019;35: 830–838.  
708 doi:10.1093/bioinformatics/bty736
- 709 20. Sher A, Niederer SA, Mirams GR, Kirpichnikova A, Allen R, Pathmanathan P, et al. A Quantitative  
710 Systems Pharmacology Perspective on the Importance of Parameter Identifiability. *B Math Biol.* 2022;84: 39.  
711 doi:10.1007/s11538-021-00982-5
- 712 21. Coope ID, Price CJ. A direct search conjugate directions algorithm for unconstrained minimization.  
713 *Anziam J.* 2000;42: 478–498. doi:10.21914/anziamj.v42i0.609
- 714 22. Hough PD, Kolda TG, Torczon VJ. Asynchronous Parallel Pattern Search for Nonlinear Optimization.  
715 *Siam J Sci Comput.* 2001;23: 134–156. doi:10.1137/s1064827599365823

- 716 23. Groenendaal W, Ortega FA, Kherlopian AR, Zygmunt AC, Krogh-Madsen T, Christini DJ. Cell-Specific  
717 Cardiac Electrophysiology Models. *Plos Comput Biol.* 2015;11: e1004242. doi:10.1371/journal.pcbi.1004242
- 718 24. Sarkar AX, Sobie EA. Regression Analysis for Constraining Free Parameters in Electrophysiological  
719 Models of Cardiac Cells. *Plos Comput Biol.* 2010;6: e1000914. doi:10.1371/journal.pcbi.1000914
- 720 25. Zaniboni M, Riva I, Cacciani F, Groppi M. How different two almost identical action potentials can be: A  
721 model study on cardiac repolarization. *Math Biosci.* 2010;228: 56–70. doi:10.1016/j.mbs.2010.08.007
- 722 26. Krogh-Madsen T, Sobie EA, Christini DJ. Improving cardiomyocyte model fidelity and utility via dynamic  
723 electrophysiology protocols and optimization algorithms. *J Physiology.* 2016;594: 2525–2536.  
724 doi:10.1113/jp270618
- 725 27. Hooke R, Jeeves TA. ``Direct Search'' Solution of Numerical and Statistical Problems. *J Acm Jacm.*  
726 1961;8: 212–229. doi:10.1145/321062.321069
- 727 28. Torczon V. On the Convergence of Pattern Search Algorithms. *Siam J Optimiz.* 1997;7: 1–25.  
728 doi:10.1137/s1052623493250780
- 729 29. Ma J, Guo L, Fiene SJ, Anson BD, Thomson JA, Kamp TJ, et al. High purity human-induced pluripotent  
730 stem cell-derived cardiomyocytes: electrophysiological properties of action potentials and ionic currents. 2011.
- 731 30. Hagiwara N, IRISAWA H, Kasanuki H, Hosoda S. Background current in sino-atrial node cells of the  
732 rabbit heart. *The Journal of physiology.* 1992;448: 53–72. doi:10.1113/jphysiol.1992.sp019029
- 733 31. Kiyosue T, Spindler AJ, Noble SJ, NOBLE D. Background inward current in ventricular and atrial cells of  
734 the guinea-pig. *Proceedings Biological sciences.* 1993;252: 65–74. doi:10.1098/rspb.1993.0047
- 735 32. Cheng H, Li J, James AF, Inada S, Choisy SCM, Orchard CH, et al. Characterization and influence of  
736 cardiac background sodium current in the atrioventricular node. *J Mol Cell Cardiol.* 2016;97: 114–24.  
737 doi:10.1016/j.yjmcc.2016.04.014
- 738 33. Tusscher KHWJ ten, Noble D, Noble PJ, Panfilov AV. A model for human ventricular tissue. *Am J*  
739 *Physiol-heart C.* 2004;286: H1573–H1589. doi:10.1152/ajpheart.00794.2003
- 740 34. Ashford JR, Colquhoun D. Lectures on Biostatistics: An Introduction to Statistics with Applications in  
741 Biology and Medicine. *J Royal Statistical Soc Ser Gen.* 1972;135: 606–606. doi:10.2307/2344687
- 742 35. Syed Z, Vigmond E, Nattel S, Leon LJ. Atrial cell action potential parameter fitting using genetic  
743 algorithms. *Medical Biological Eng Comput.* 2005;43: 561–571. doi:10.1007/bf02351029
- 744 36. Guo T, Abed AA, Lovell NH, Dokos S. Optimisation of a Generic Ionic Model of Cardiac Myocyte  
745 Electrical Activity. *Comput Math Method M.* 2013;2013: 706195. doi:10.1155/2013/706195
- 746 37. Beeler GW, Reuter H. Reconstruction of the action potential of ventricular myocardial fibres. *J Physiology.*  
747 1977;268: 177–210. doi:10.1113/jphysiol.1977.sp011853
- 748 38. Faber GM, Rudy Y. Action Potential and Contractility Changes in  $[Na^+]_i$  Overloaded Cardiac Myocytes:  
749 A Simulation Study. *Biophys J.* 2000;78: 2392–2404. doi:10.1016/s0006-3495(00)76783-x

- 750 39. Powell T, Twist VW. A rapid technique for the isolation and purification of adult cardiac muscle cells  
751 having respiratory control and a tolerance to calcium. *Biochem Bioph Res Co.* 1976;72: 327–333.  
752 doi:10.1016/0006-291x(76)90997-9
- 753 40. Sakmann B, Neher E. Patch Clamp Techniques for Studying Ionic Channels in Excitable Membranes.  
754 *Annu Rev Physiol.* 1984;46: 455–472. doi:10.1146/annurev.ph.46.030184.002323
- 755 41. Cha CY, Himeno Y, Shimayoshi T, Amano A, Noma A. A novel method to quantify contribution of  
756 channels and transporters to membrane potential dynamics. *Biophys J.* 2009;97: 3086–3094.  
757 doi:10.1016/j.bpj.2009.08.060
- 758 42. Winslow RL, Walker MA, Greenstein JL. Modeling calcium regulation of contraction, energetics,  
759 signaling, and transcription in the cardiac myocyte. *Wiley Interdiscip Rev Syst Biology Medicine.* 2016;8: 37–  
760 67. doi:10.1002/wsbm.1322
- 761 43. Hilgemann DW, Feng S, Nasuhoglu C. The Complex and Intriguing Lives of PIP2 with Ion Channels and  
762 Transporters. *Sci Stke.* 2001;2001: re19. doi:10.1126/stke.2001.111.re19
- 763 44. Suh B-C, Hille B. PIP2 Is a Necessary Cofactor for Ion Channel Function: How and Why? *Biophysics.*  
764 2008;37: 175–195. doi:10.1146/annurev.biophys.37.032807.125859
- 765 45. Sasaki N, Mitsuiye T, Wang Z, Noma A. Increase of the delayed rectifier K<sup>+</sup> and Na<sup>(+)</sup>-K<sup>+</sup> pump currents  
766 by hypotonic solutions in guinea pig cardiac myocytes. *Circ Res.* 2018;75: 887–895.  
767 doi:10.1161/01.res.75.5.887
- 768 46. Hammami S, Willumsen NJ, Olsen HL, Morera FJ, Latorre R, Klaerke DA. Cell volume and membrane  
769 stretch independently control K<sup>+</sup> channel activity: Cell volume, membrane stretch and K<sup>+</sup> channel activity. *J*  
770 *Physiology.* 2009;587: 2225–2231. doi:10.1113/jphysiol.2008.163550
- 771 47. Peyronnet R, Nerbonne JM, Kohl P. Cardiac Mechano-Gated Ion Channels and Arrhythmias. *Circ Res.*  
772 2016;118: 311–329. doi:10.1161/circresaha.115.305043
- 773 48. Gao J, Yun T, Xie X-L, Zhao J, Liu C, Sheng Y, et al. Losartan inhibits hyposmotic-induced increase of  
774 IKs current and shortening of action potential duration in guinea pig atrial myocytes. *Anatol J Cardiol.*  
775 2020;23: 35–40. doi:10.14744/anatoljcardiol.2019.75332
- 776 49. Cannell MB, Kong CHT. Local control in cardiac E–C coupling. *J Mol Cell Cardiol.* 2012;52: 298–303.  
777 doi:10.1016/j.yjmcc.2011.04.014
- 778 50. Bers DM. Calcium Cycling and Signaling in Cardiac Myocytes. *Annu Rev Physiol.* 2008;70: 23–49.  
779 doi:10.1146/annurev.physiol.70.113006.100455
- 780 51. Greenstein JL, Hinch R, Winslow RL. Mechanisms of Excitation-Contraction Coupling in an Integrative  
781 Model of the Cardiac Ventricular Myocyte. *Biophys J.* 2006;90: 77–91. doi:10.1529/biophysj.105.065169
- 782 52. Negroni JA, Lascano EC. Simulation of steady state and transient cardiac muscle response experiments  
783 with a Huxley-based contraction model. *Journal of molecular and cellular cardiology.* 2008;45: 300–312.  
784 doi:10.1016/j.yjmcc.2008.04.012

- 785 53. Timmermann V, Edwards AG, Wall ST, Sundnes J, McCulloch AD. Arrhythmogenic Current Generation  
786 by Myofilament-Triggered Ca<sup>2+</sup> Release and Sarcomere Heterogeneity. *Biophys J*. 2019;117: 2471–2485.  
787 doi:10.1016/j.bpj.2019.11.009
- 788 54. Niederer SA, Campbell KS, Campbell SG. A short history of the development of mathematical models of  
789 cardiac mechanics. *J Mol Cell Cardiol*. 2019;127: 11–19. doi:10.1016/j.yjmcc.2018.11.015
- 790 55. Hagiwara N, Irisawa H, Kameyama M. Contribution of two types of calcium currents to the pacemaker  
791 potentials of rabbit sino-atrial node cells. *J Physiology*. 1988;395: 233–253.  
792 doi:10.1113/jphysiol.1988.sp016916
- 793 56. Zhou Z, Lipsius SL. T-Type Calcium Current in Latent Pacemaker Cells Isolated from Cat Right Atrium. *J*  
794 *Mol Cell Cardiol*. 1994;26: 1211–1219. doi:10.1006/jmcc.1994.1139
- 795 57. Guo J, Ono K, Noma A. A sustained inward current activated at the diastolic potential range in rabbit sino-  
796 atrial node cells. *J Physiology*. 1995;483: 1–13. doi:10.1113/jphysiol.1995.sp020563
- 797 58. Toyoda F, Mesirca P, Dubel S, Ding W-G, Striessnig J, Mangoni ME, et al. CaV1.3 L-type Ca<sup>2+</sup> channel  
798 contributes to the heartbeat by generating a dihydropyridine-sensitive persistent Na<sup>+</sup> current. *Sci Rep-uk*.  
799 2017;7: 7869. doi:10.1038/s41598-017-08191-8
- 800 59. Toyoda F, Wei-Guang D, Matsuura H. Heterogeneous functional expression of the sustained inward Na<sup>+</sup>  
801 current in guinea pig sinoatrial node cells. *Pflügers Archiv - European J Physiology*. 2018;470: 481–490.  
802 doi:10.1007/s00424-017-2091-y
- 803 60. Guinamard R, Bouvagnet P, Hof T, Liu H, Simard C, Sallé L. TRPM4 in cardiac electrical activity.  
804 *Cardiovasc Res*. 2015;108: 21–30. doi:10.1093/cvr/cvv213
- 805 61. Doss MX, Diego JMD, Goodrow RJ, Wu Y, Cordeiro JM, Nesterenko VV, et al. Maximum diastolic  
806 potential of human induced pluripotent stem cell-derived cardiomyocytes depends critically on I(Kr). Barbuti  
807 A, editor. *Plos One*. 2012;7: e40288. doi:10.1371/journal.pone.0040288
- 808 62. Ishihara K, Yan D, Yamamoto S, Ehara T. Inward rectifier K<sup>+</sup> current under physiological cytoplasmic  
809 conditions in guinea-pig cardiac ventricular cells. *J Physiology*. 2002;540: 831–841.  
810 doi:10.1113/jphysiol.2001.013470
- 811 63. Takahashi K, Yamanaka S. Induction of pluripotent stem cells from mouse embryonic and adult fibroblast  
812 cultures by defined factors. *Cell*. 2006;126: 663–676. doi:10.1016/j.cell.2006.07.024
- 813 64. Nakagawa M, Koyanagi M, Tanabe K, Takahashi K, Ichisaka T, Aoi T, et al. Generation of induced  
814 pluripotent stem cells without Myc from mouse and human fibroblasts. *Nat Biotechnol*. 2008;26: 101–106.  
815 doi:10.1038/nbt1374
- 816 65. Yang L, Soonpaa MH, Adler ED, Roepke TK, Kattman SJ, Kennedy M, et al. Human cardiovascular  
817 progenitor cells develop from a KDR<sup>+</sup> embryonic-stem-cell-derived population. *Nature*. 2008;453: 524–528.  
818 doi:10.1038/nature06894

819

820

## Supplementary Files

This is a list of supplementary files associated with this preprint. Click to download.

- [SupplementalMaterialV8.pdf](#)